

# *In vivo* Three-Dimensional Superresolution Fluorescence Tracking using a Double-Helix Point Spread Function

Matthew D. Lew<sup>a,b</sup>, Michael A. Thompson<sup>b</sup>, Majid Badieirostami<sup>b</sup>, and W. E. Moerner<sup>\*b</sup>  
 Departments of <sup>a</sup>Electrical Engineering and <sup>b</sup>Chemistry, Stanford University, Stanford, CA 94305

## ABSTRACT

The point spread function (PSF) of a widefield fluorescence microscope is not suitable for three-dimensional super-resolution imaging. We characterize the localization precision of a unique method for 3D superresolution imaging featuring a double-helix point spread function (DH-PSF). The DH-PSF is designed to have two lobes that rotate about their midpoint in any transverse plane as a function of the axial position of the emitter. In effect, the PSF appears as a double helix in three dimensions. By comparing the Cramer-Rao bound of the DH-PSF with the standard PSF as a function of the axial position, we show that the DH-PSF has a higher and more uniform localization precision than the standard PSF throughout a 2  $\mu\text{m}$  depth of field. Comparisons between the DH-PSF and other methods for 3D super-resolution are briefly discussed. We also illustrate the applicability of the DH-PSF for imaging weak emitters in biological systems by tracking the movement of quantum dots in glycerol and in live cells.

**Keywords:** superresolution, three-dimensional microscopy, fluorescence microscopy, single-particle tracking, quantum dot

## 1. INTRODUCTION

### 1.1 Fluorescence microscopy and superlocalization in two dimensions

Since its invention in 1911,<sup>1</sup> optical fluorescence microscopy has become ubiquitous in cell biology studies. Because it uses light to probe a sample in a relatively non-invasive and non-perturbative fashion with high signal-to-noise ratios, fluorescence microscopy can be used to directly observe structures and dynamics within living cells. As the technique was developed and used for studying nanoscale objects, the optical diffraction limit quickly became an obstacle. The Rayleigh criterion dictates that the diffraction-limited resolution  $d$  of an optical microscope is given by

$$d = \frac{0.61\lambda}{NA}, \quad (1)$$

where  $\lambda$  is the emission wavelength of the emitter and  $NA$  is the numerical aperture of the microscope objective. This resolution limit is  $\sim 250$  nm for optical wavelengths, and features separated by less than this distance are unresolvable.

Fortunately, images of single nanoscale emitters can be fit to extract the  $xy$  position of the object with nanometer precision.<sup>2,3</sup> This localization precision  $\sigma$  scales roughly as  $s/N^{1/2}$  for photon-limited shot noise, where  $s$  is the standard deviation of the microscope's point spread function (PSF) and  $N$  is the number of photons detected. In this way, the location of a point emitter can be determined to a much greater precision than the diffraction-limited resolution of an optical system. This "superlocalization" property is well known in many areas of science,<sup>4</sup> and this technique has been applied in single-molecule tracking studies<sup>5,6</sup> with great success.

### 1.2 Single-Molecule Active-Control Microscopy (SMACM)

Superlocalization of a biological structure requires a dense fluorescent labeling of that structure, and any nanoscale detail will be blurred out by the overlap of the PSFs from each of the emitters. This "high concentration" problem in single-molecule imaging can be overcome with Single-Molecule Active-Control Microscopy (SMACM),<sup>7</sup> which enables high-resolution imaging of dense ensembles of fluorescent molecules. SMACM utilizes the active control of photoactivatable or photoswitchable fluorescent molecules to keep the concentration of activated emitters low at any instant in time. This is usually accomplished by using a secondary control wavelength to turn on only a subset of the emitters such that the emitter density is sparse. Each emitter in this subset is then localized, and its position is recorded (see Figure 1A-C).

\*wmoerner@stanford.edu; phone (650) 723-1727; fax (650) 725-0259; <http://www.stanford.edu/group/moerner/>

After localization, a new cycle of activation and localization is performed on another subset of emitters, and this process is repeated until the positions of all of the fluorescent labels have been determined. By combining the fitted positions of emitters from each cycle, one can attain a high-resolution image of the desired biological structure (see Figure 1E). Methods of active control include photoswitching, reversible photoblinking, or triplet state formation. It is important to note that other solutions exist to the “high concentration” problem, such as spectral selectivity.<sup>8</sup> However, recently, SMACM has been successfully applied to biological systems, denoted by the acronyms PALM, F-PALM, and STORM.<sup>9-11</sup>

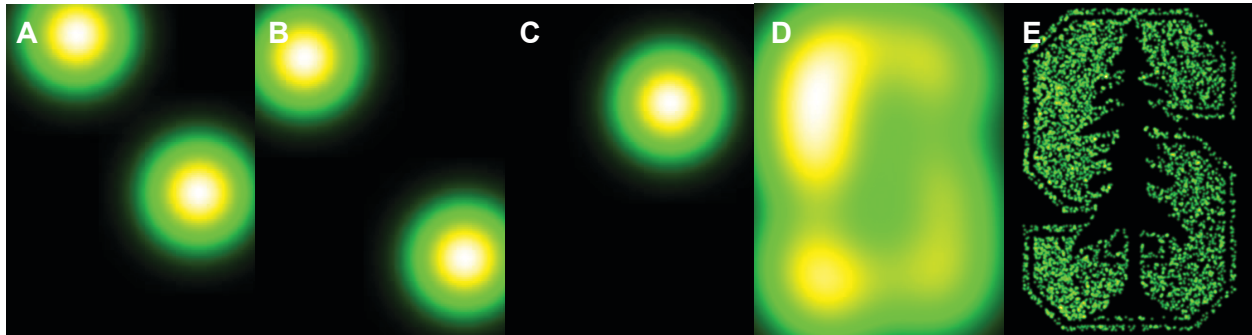


Figure 1. Simulation of SMACM imaging concept. (A-C) Diffraction-limited images of low concentrations of active emitters labeling a sample structure. The emitter locations in these images can be fit to a precision much better than the diffraction-limited spot size. (D) Diffraction-limited image of all labels emitting simultaneously on a sample structure. Note that the structure details are blurred by diffraction. (E) SMACM image of the sample structure, created by summing all fitted emitter locations collected during repeated activation and localization cycles. Note that the resolution improvement yields a clearly resolved structure. The resolution improvement between (D) and (E), which is approximately a factor of 32, is typical of cases where the single emitter produce about 1000 detected photons.

### 1.3 Superlocalization in three dimensions

The above methods, until recently, have been restricted to two-dimensions for two reasons: (1) the PSF of a conventional microscope is symmetric about the focal plane (see Figure 2A); thus, a molecule  $z$  nm above the focal plane cannot be distinguished from a molecule  $z$  nm below the focal plane, and (2) the PSF of a conventional microscope contains very little information about the axial position of an emitter that lies within a few hundred nanometers of the focal plane,<sup>12, 13</sup> meaning that the  $z$  localization precision of the standard PSF is poor for emitters that lie near the focal plane. Recently, several solutions to these problems have been developed, namely astigmatism,<sup>14-16</sup> imaging in two focal planes,<sup>13, 17-19</sup> and interferometry.<sup>20, 21</sup> In addition, fast 3D particle tracking has been performed using confocal microscopy<sup>22-24</sup> and two rotating laser beams.<sup>24</sup>

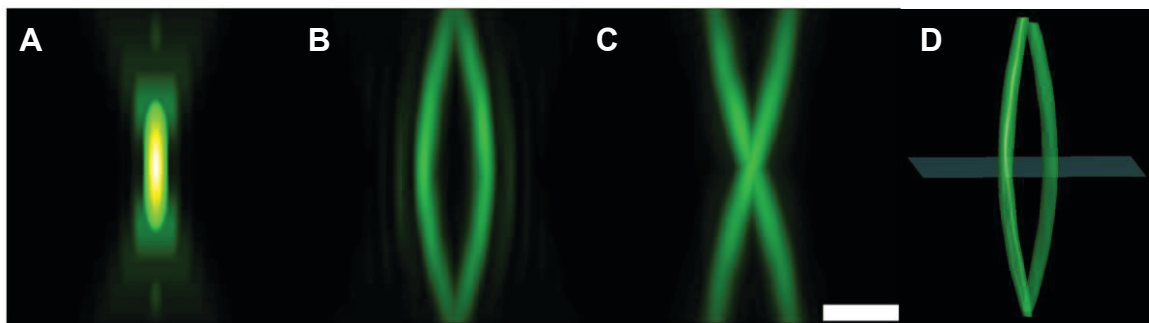


Figure 2. Simulations comparing the conventional PSF and DH-PSF. (A)  $xz$  profile of a conventional PSF. This is the same as a  $yz$  profile since the PSF is radially symmetric. (B)  $xz$  profile of the DH-PSF. (C)  $yz$  profile of the DH-PSF. Note that the DH-PSF contains more information about the  $z$  location of an emitter since its gradient is a stronger function of  $z$ . The intensities of the PSFs are plotted on the same color scale, which is saturated to show the DH-PSF more clearly. The scale bar height represents 100 nm in the axial direction (object space), while the scale bar length represents 1  $\mu\text{m}$  in the transverse dimension. (D) Three-dimensional isosurface rendering of the DH-PSF, with the focal plane included for reference. The simulation uses an emitter wavelength of  $\lambda=633$  nm and a 100 $\times$  oil-immersion objective ( $n_{\text{oil}}=1.518$ ).

We have recently demonstrated the superlocalization of single-molecules<sup>25</sup> and quantum dots<sup>26</sup> in three dimensions using the double-helix point spread function (DH-PSF), as shown in Figure 2B-D. The DH-PSF was developed and provided by R. Piestun and S.R.P. Pavani at the University of Colorado.<sup>27</sup> With a widefield fluorescence microscope exhibiting the DH-PSF, point emitters appear as two lobes that rotate about one another as a function of the axial position of the emitter. The midpoint between the two lobes corresponds to the  $xy$  position of the emitter, while the angle between the two lobes corresponds to the  $z$  position of the emitter. In this manner, the three-dimensional location of point-like emitters can be easily calculated. Combining the DH-PSF with photoactivatable fluorophores yields a three-dimensional variant of SMACM termed double-helix photoactivated localization microscopy (DH-PALM).

The DH-PSF has several distinct advantages over other methods when used for three-dimensional localization. It has a high Fisher information content in all three dimensions that is relatively constant over a  $2\ \mu\text{m}$  depth of field.<sup>26</sup> This implies that the localization precision attainable with the DH-PSF is independent of the location of a fluorescent emitter. Furthermore, the shape of the DH-PSF is largely invariant over the entire depth of field. Instead of using the precise shape of an image to determine the  $xyz$  location of an emitter, as is the case for the astigmatism and multiplane methods, the midpoint and angle between the two lobes yields the three-dimensional location of an emitter. Finding the position of a peaked function is often easier than extracting the form of a function under low signal-to-noise conditions.

Studies using the DH-PSF for superlocalization of bright objects such as  $1\ \mu\text{m}$  fluorescent beads<sup>28</sup> and point scatterers<sup>29</sup> have been demonstrated. However, many SMACM experiments use relatively dim fluorescent protein labels that emit an order of magnitude fewer photons than the examples noted above. Here, we show the tracking of quantum dots in glycerol and within COLO205 cells in three-dimensions using the DH-PSF. We begin by describing the experimental setup and fitting algorithm in detail, including typical calibration curves used in our experiments. We also discuss the use of fiducials for removal of stage drift. The computational model of the system that is used to calculate the Fisher information content of the DH-PSF is then described. We compare the Fisher information content of the standard PSF versus the DH-PSF. Finally, we demonstrate *in vivo* tracking studies of quantum dots performed within live cells using the DH-PSF.

## 2. METHODS

### 2.1 Physical setup

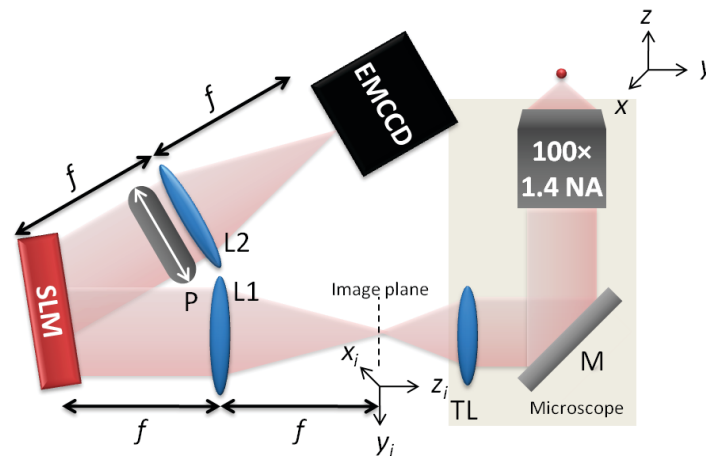


Figure 3. Schematic of the DH-PSF setup. A  $4f$  imaging system is placed in the detection path of a conventional fluorescence microscope consisting of a  $100\times$   $1.4\ \text{NA}$  oil-immersion objective, mirror (M), and a tube lens (TL). The magnified image relayed from the microscope is input into the  $4f$  system consisting of two lenses (L1 and L2) placed a distance  $2f$  ( $f=15\ \text{cm}$ ) apart. A phase-only liquid crystal spatial light modulator with a DH-PSF mask is placed in the Fourier plane of the  $4f$  system in order to convolve the microscope image with the DH-PSF. A polarizer (P) within the  $4f$  system rejects unmodulated light. An electron-multiplying charge-coupled device (EMCCD) camera detects the resulting image.

The conventional PSF of a fluorescence microscope (Olympus IX71) with a  $100\times$  1.4 NA oil-immersion objective (Olympus UPlanSApo  $100\times/1.40$ ) is convoluted with the DH-PSF using an all-optical  $4f$  imaging system in the detection path of the microscope (see Figure 3). The  $4f$  imaging system is composed of two achromatic lenses (Edmund Optics NT32-886,  $f=15$  cm) with a reflective liquid crystal phase-only spatial light modulator (SLM, Boulder Nonlinear Systems XY phase series) placed at a slight angle in the Fourier plane for optical convenience. In Fourier plane of the  $4f$  system, the Fourier transform of the sample image is multiplied by the phase mask of the SLM. This product is then Fourier transformed by the second lens, thereby restoring a real-space image onto an electron-multiplying charge-coupled device camera (EMCCD, Andor Ixon<sup>+</sup>). The phase mask of the SLM is designed to be the Fourier transform of the DH-PSF. Thus, the net effect of the  $4f$  imaging system is to convolve the microscope image with the DH-PSF. Since the SLM can only modulate vertically polarized light, a polarizer is placed in the  $4f$  system to reject unmodulated light. This creates a significant loss in photon efficiency ( $\sim 50\%$ ). However, it is important to note that this loss is due to this specific implementation of the DH-PSF and can be easily avoided.<sup>30</sup>

## 2.2 Data analysis

The phase mask used to create the DH-PSF is a superposition of Laguerre-Gaussian modes derived from an optimization scheme,<sup>27</sup> and since the DH-PSF is created by Fourier transforming the phase mask, an analytic expression of the DH-PSF does not exist. However, any transverse slice of the DH-PSF can be approximated by an eleven-parameter double Gaussian function, which can be written as

$$U(u, v) = A_1 \exp\left[-\frac{(u - \mu_{x1})^2}{2\sigma_{x1}^2}\right] \exp\left[-\frac{(v - \mu_{y1})^2}{2\sigma_{y1}^2}\right] + A_2 \exp\left[-\frac{(u - \mu_{x2})^2}{2\sigma_{x2}^2}\right] \exp\left[-\frac{(v - \mu_{y2})^2}{2\sigma_{y2}^2}\right] + B, \quad (2)$$

where  $(u, v)$  are coordinates on the EMCCD camera;  $A_1$  is the amplitude of the first lobe;  $A_2$  is the amplitude of the second lobe;  $(\mu_{x1}, \mu_{y1})$  is the location of the first lobe;  $(\mu_{x2}, \mu_{y2})$  is the location of the second lobe;  $\sigma_{x1}$ ,  $\sigma_{y1}$ ,  $\sigma_{x2}$ , and  $\sigma_{y2}$  are widths of the lobes; and  $B$  is the amplitude of the background. The MATLAB function `fminsearch` is used to compute these parameters by minimizing the mean-square error between Equation 2 and the measured data (a  $19 \times 19$  pixel box is used around the emitter of interest). Although an eleven-parameter function is difficult to fit without sufficiently accurate initial parameters, the use of eleven parameters is robust against various aberrations in the physical setup that cause asymmetric lobe amplitudes and shapes. Once the DH-PSF has been fit to a double Gaussian function, the  $x$  and  $y$  locations of the emitter are determined by calculating the midpoint of the two lobes. The  $z$  location of the emitter is calculated by measuring the angle between the two lobes and comparing this angle to a measured  $z$  calibration curve.

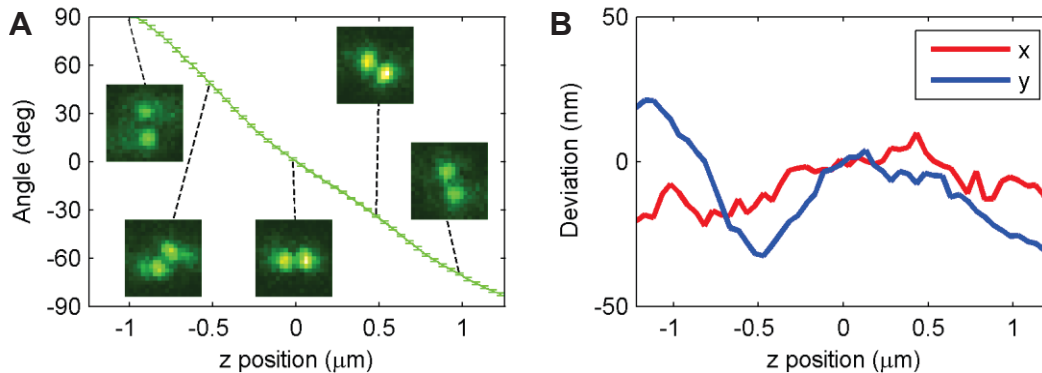


Figure 4. Typical calibration curves for the DH-PSF setup. (A) Angle versus  $z$  calibration curve with insets showing the rotation of the DH-PSF as a function of  $z$ . All of the inset images are plotted with the same color scale to show relative intensity. The tiny error bars show the standard deviation in the measured angle at each  $z$  position, which translates into a  $z$  localization precision of  $\sim 10$  nm throughout a depth of field of  $2 \mu\text{m}$ . (B) Deviation in the midpoint ( $xy$ ) of the DH-PSF as a function of  $z$ . This deviation is constant over the entire lateral field of view for well-aligned systems. Data from both plots were collected from a  $200$  nm fluorescent bead producing an average of  $10000$  detected photons/frame at  $\lambda=645$  nm. This bead was scanned at intervals of  $50$  nm in the axial direction with  $50$  acquisitions per each step.

The  $z$  calibration curve (see Figure 4A) is generated by measuring the rotation angle of the DH-PSF as a function of  $z$  with a piezoelectric objective  $z$ -scanner (Physik Instrumente PIFOC). For the calibration curve shown in Figure 4A, a 200 nm fluorescent bead emitting at  $\lambda=645$  nm was moved in 50 nm steps in the axial direction, and fifty acquisitions were used at each step to determine the angle of the lobes at that position. This curve is then used to translate the angle between the lobes of the DH-PSF into  $z$  position.

Unfortunately, the midpoint of the DH-PSF is also a weak function of  $z$  (see Figure 4B). As the  $z$  position of the emitter is scanned through the depth of field, the measured midpoint between the two lobes translates because of slight misalignments of the lenses and SLM in the  $4f$  imaging system. This midpoint can be measured as a function of  $z$  using the same scanning method used in Figure 4A; thus, data for both curves in Figure 4 are measured simultaneously from the same bead. If the system is well aligned, the deviation of the center of the DH-PSF as a function of  $z$  is constant regardless of the emitter's location in the  $xy$  plane. Thus, any systematic deviation in the midpoint of the DH-PSF can be removed from experimental data using the calibration curve in Figure 4B. It is important to note that stage drift is negligible in Figure 4B because the microscope stage was allowed to settle for several hours in a temperature-controlled laboratory before the data was taken.

However, in many biological experiments, stage equilibration may not be possible due to the time constraints imposed by live cell imaging. Thus, the microscope stage will drift during an experiment because of thermal and mechanical fluctuations, thereby introducing localization artifacts. A typical method to correct drift during an experiment is to use a bright fiduciary, such as a fluorescent bead, in the sample as a reference for stage drift. A typical track of a bright fiduciary as a function of time in a live-cell imaging experiment with no prior setup equilibration is shown in Figure 5. The movement of this fiduciary is subtracted from the measured locations of emitters within a sample, yielding data that is free of stage drift artifacts. Since the fiduciary is usually much brighter than the emitters of interest, the localization error introduced by using the fiduciary is negligible compared to the error contributed by other noise sources.

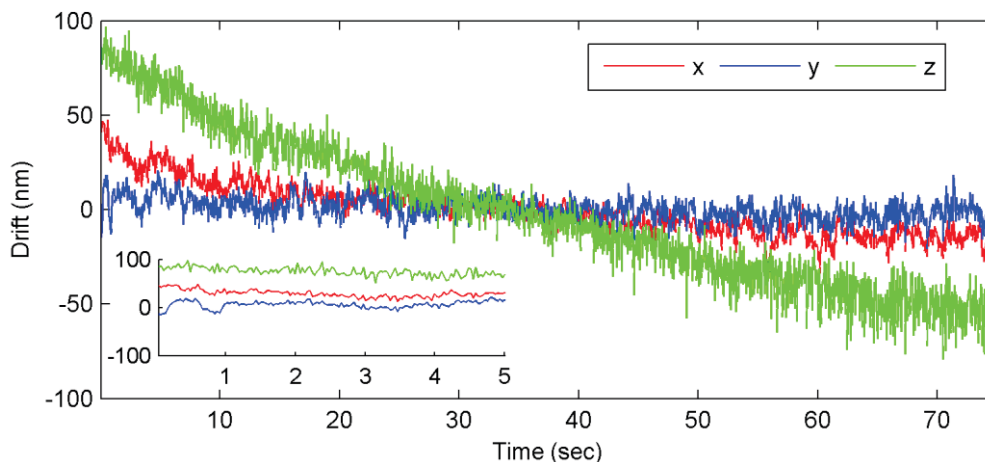


Figure 5. Typical three-dimensional track of a bright fiduciary during a live-cell localization experiment. The position of the fiduciary was recorded every 35 ms for  $\sim 75$  seconds. The fiduciary is a 100 nm fluorescent bead emitting approximately 20000 photons per acquisition. The inset shows the first 5 seconds of the track.

Using a double Gaussian function to approximate the DH-PSF is computationally efficient while yielding satisfactory localization precision for high signal-to-noise ratios. However, there is a small but significant deviation between the shape of the DH-PSF and the corresponding fit to a double Gaussian function. In particular, the tails of the DH-PSF form an extra haze around the two lobes that scales with the brightness of the emitter (see Figure 6). This haze is more severe along the axis connecting the two lobes than the orthogonal axis. To the double Gaussian fitting algorithm, the haze effectively functions as a source of background noise, since the haze is not used by the algorithm to localize emitters. If additional precision is desired, a more accurate model of the DH-PSF, such as an experimentally measured PSF,<sup>31</sup> could be used for the fitting algorithm at the expense of computational speed.

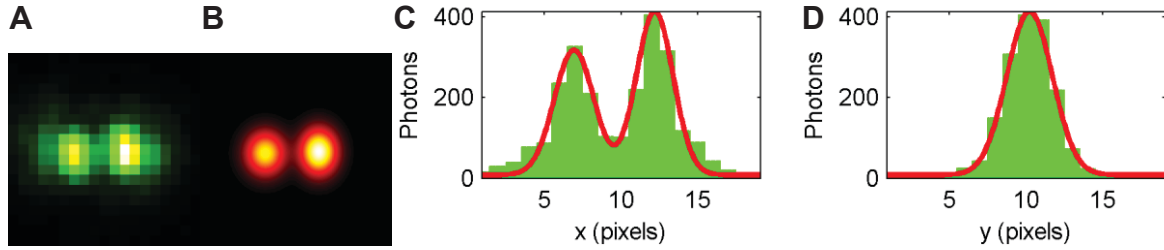


Figure 6. Comparing the DH-PSF and double Gaussian fit. (A) Experimentally measured DH-PSF using a 200 nm fluorescent bead as an emitter. Fifty frames of this bead producing approximately 8100 detected photons/frame were averaged together to create this image. Note that the two lobes are asymmetric in both intensity and shape. (B) Double Gaussian fit of the image in (A). (C) Profile of the experimentally measured DH-PSF (green) superimposed with the double Gaussian fit (red), viewed along the  $y$ -axis. This plot clearly shows the haze surrounding the two lobes of the DH-PSF. (D) Same as (C), except viewed along the  $x$ -axis. There is virtually no haze surrounding the DH-PSF along this axis. Pixel size in all plots is  $160 \times 160$  nm in object space, which corresponds to  $15 \times 15$   $\mu\text{m}$  on the EMCCD camera.

### 2.3 Theoretical model of imaging system

A computational model of the microscope and  $4f$  imaging system is necessary for simulating the DH-PSF as well as calculating the Fisher information present in the DH-PSF. Specifically, the image of the DH-PSF as measured by the EMCCD camera must be calculated as a function of the location of a point source in the sample volume of the objective lens (see Figure 3). The microscope maps the location of the point source in the object plane  $(x, y, z)$  to a location in the image plane  $(x_i, y_i, z_i)$ , which is given by

$$\begin{aligned} x_i &= M x \\ y_i &= M y \\ z_i &= \frac{M^2}{n_{oil}} z \end{aligned} \quad (3)$$

where  $z = 0$  defines the focal plane of the objective lens,  $f + z_i$  gives the distance between the point source and the first lens in the  $4f$  system,  $M$  is the magnification of the objective lens, and  $n_{oil}$  is the index of refraction of the immersion oil. The index of refraction of the immersion oil must be taken into account since the sample is immersed in oil, while the image of the sample is formed in air.

Once the location of the point source is determined in the image plane, it is relatively straightforward to calculate the image of the DH-PSF on the EMCCD camera. Assuming that the numerical aperture of the system is sufficiently large, the Fourier transform of the point source in the image plane is a uniform intensity distribution at the SLM. This distribution is modulated by the phase mask of the spatial light modulator, which is then Fourier transformed by lens L2 onto the EMCCD camera. Thus, the intensity image of the DH-PSF  $U(u, v)$  is given by<sup>32</sup>

$$U(u, v) = \left| \frac{1}{i\lambda f} F \left\{ \exp \left[ i \frac{\pi z_i}{\lambda f^2} \left( (u - x_i)^2 + (v - y_i)^2 \right) \right] t_A \left( \frac{u - x_i}{\lambda f}, \frac{v - y_i}{\lambda f} \right) \right\} \right|^2, \quad (4)$$

where  $\lambda$  is the wavelength of the point emitter,  $f$  is the focal length of the lenses in the  $4f$  system,  $(x_i, y_i, z_i)$  is the location of the point source image in the image plane,  $(u, v)$  are coordinates on the EMCCD camera,  $F$  is the two-dimensional Fourier transform operator, and  $t_A(x, y)$  is the transmittance function of the phase mask. It is important to note that this model assumes a monochromatic point emitter. This assumption is largely for computational speed and convenience, and we find that this model predicts the behavior of the DH-PSF with reasonable accuracy.

### 2.4 Fisher information calculation

One of the fundamental issues in single-molecule microscopy is the precision with which the position of a single molecule can be estimated. Localization precision is of significant interest in single-molecule data analysis and when comparing different microscopy techniques regardless of estimation algorithms. Due to the stochastic nature of the

acquired data in single-molecule microscopy, the estimation of the location of the single-molecule emitter is recast as a statistical problem. Here, we use the tools of statistical estimation theory and specifically Fisher information analysis to find the fundamental limit of the 3D localization precision of a single molecule.

Fisher information is a quantity that plays a central role in the statistical estimation theory.<sup>33, 34</sup> It describes how much information a likelihood function contains about a parameter. In our case, the likelihood function is the DH-PSF (regarded as the probability distribution for detection of photons) and the parameters we are concerned with are the lateral and axial positions of the emitter. The inverse of the Fisher information matrix is called the Cramer-Rao bound (CRB), which is the lowest possible position estimation variance that can be achieved when estimating the position of a point emitter with an unbiased estimator (i.e., any estimation procedure whose mean produces the correct result), i.e.,  $\sigma^2 \geq \mathbf{I}^{-1}(\theta)$ . The square root of the CRB is the lower limit of localization precision. It is a fundamental parameter for evaluating the precision of different estimators, and it is a useful bound for comparing different microscopy techniques.

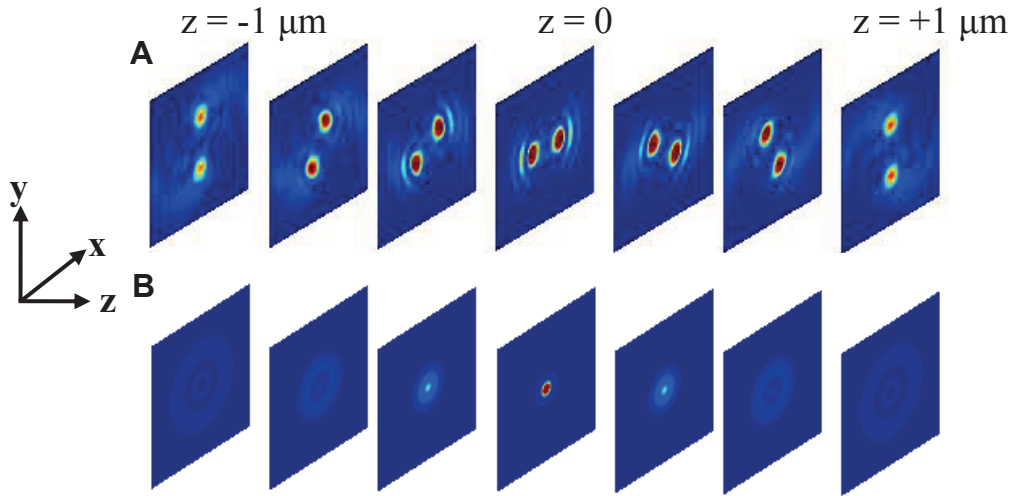


Figure 7. The numerically obtained (A) DH-PSF and (B) standard PSF images versus axial distance for  $\lambda = 633$  nm which are used as the image function  $q_{z_0}(x, y)$  in the Fisher information calculation.

In order to calculate the smallest value of the localization precision, we have adopted the same methodology described previously,<sup>3, 13</sup> with the only difference that the image function, i.e.  $q_{z_0}(x, y)$ , is replaced by the DH-PSF shown in Figure 7A. Figure 7B shows the standard PSF, which is the simple Airy profile characteristic of conventional fluorescence microscopy. The Fisher information matrix is calculated as

$$\mathbf{I}(\theta) = \begin{bmatrix} N \int_{\mathbb{R}^2} \frac{1}{q_{z_0}(x, y)} \left( \frac{\partial q_{z_0}(x, y)}{\partial x} \right)^2 dx dy & 0 & 0 \\ 0 & N \int_{\mathbb{R}^2} \frac{1}{q_{z_0}(x, y)} \left( \frac{\partial q_{z_0}(x, y)}{\partial y} \right)^2 dx dy & 0 \\ 0 & 0 & N \int_{\mathbb{R}^2} \frac{1}{q_{z_0}(x, y)} \left( \frac{\partial q_{z_0}(x, y)}{\partial z} \right)^2 dx dy \end{bmatrix}, \quad (5)$$

where  $q_{z_0}(x, y)$  describes the image of a single molecule at unit magnification that is located at  $(0, 0, z_0)$  in the object space. However, several nonideal effects need to be modeled in order to produce Fisher information calculations that reflect experimental observations. We include two major effects in our calculation. The first is pixelation, which is due to the finite sized pixels of the EMCCD camera. The second and more significant effect is background noise, which arises from any fluorescent object that is not the emitter of interest. These experimental effects lead to a modification of the description of the stochastic data generation process, and they have been previously implemented in the Fisher

information theoretical analysis of conventional microscopy techniques.<sup>3, 13</sup> Here, we extend the same analysis to the DH-PSF technique. For a pixelated detector with additive Poisson noise with mean  $\beta$  counts per pixel, the Fisher information matrix is calculated as follows:

$$\mathbf{I}(\theta) = \sum_{k=1}^{N_p} \frac{1}{\mu_\theta(k) + \beta} \left( \frac{\partial \mu_\theta(k)}{\partial \theta} \right)^T \frac{\partial \mu_\theta(k)}{\partial \theta} \quad \theta = (x_0, y_0, z_0) \in \Theta, \quad (6)$$

where  $\mu_\theta(k) = N \int_{C_k} \frac{1}{M^2} q_{z_0} \left( \frac{x}{M} - x_0, \frac{y}{M} - y_0 \right) dx dy$ . Here  $\Theta$  denotes the parameter space,  $N_p$  denotes the number of pixels,  $N$  denotes the number of photons,  $C_k$  is the region in the  $xy$  plane occupied by the  $k^{\text{th}}$  pixel,  $M$  denotes the lateral magnification of the microscope,  $(x_0, y_0, z_0)$  denotes the 3D location of the single molecule in the object space.

### 3. RESULTS AND DISCUSSION

#### 3.1 Comparison between the standard PSF and the DH-PSF for three-dimensional localization

Here, we use the mathematical analysis given in Section 2.4 to calculate the localization precision of the DH-PSF and compare it with the standard PSF. In our calculation, we have used  $M = 100$ ,  $N_p = 625$  pixels (i.e., array of  $25 \times 25$  pixels) with square pixels of width 160 nm, and additive Poisson noise with a mean value of  $\beta = 2$  photons/pixel for 1000 photons present in the DH-PSF. Other noise sources are assumed to be negligible and are not included in our calculation. In addition, the refractive index of the object space medium is set to  $n_{oil} = 1.518$  to account for the effect of immersion oil in our setup. It is noteworthy that unlike the standard PSF there is no closed-form formula for the DH-PSF. Therefore, all our results are numerically calculated from the 3D sampled function in Figure 7A, which was computed from the DH-PSF phase mask using the model described in Section 2.3.

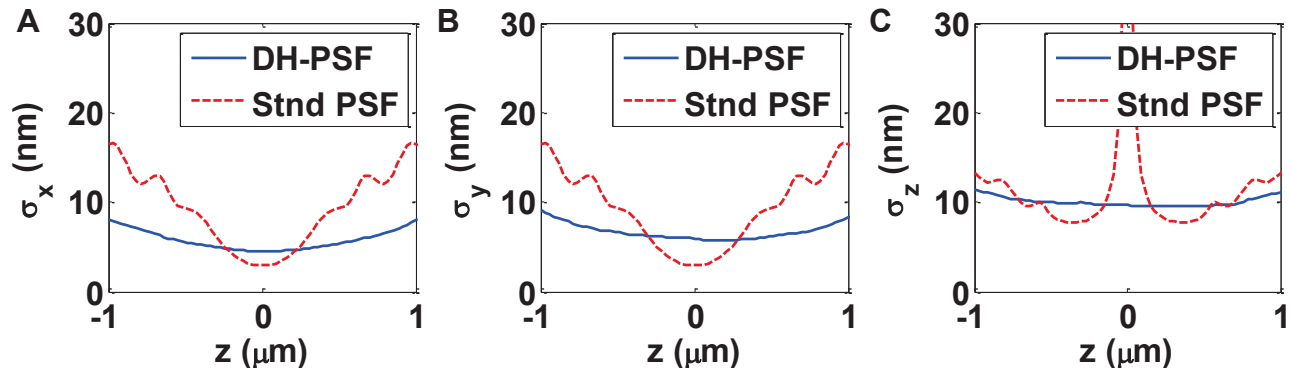


Figure 8. Comparison of the Cramer-Rao bound for the parameters (A)  $x$ , (B)  $y$ , and (C)  $z$  between the DH-PSF and standard PSF. Here, we denote  $\text{CRB}_x$  by  $\sigma_x$ ,  $\text{CRB}_y$  by  $\sigma_y$ , and  $\text{CRB}_z$  by  $\sigma_z$ . These quantities represent the best possible localization precision attainable for these point spread functions with a given amount of detected photons and noise. In this calculation, we have used  $N = 1000$  photons and a background Poisson noise with mean value of  $\beta = 2$  photons/pixel. In addition, the refractive index of the object space medium is set to  $n_{oil} = 1.518$  to account for the effect of immersion oil in our setup.

Figure 8 compares the localization precision of the DH-PSF with the standard PSF as a function of the axial position  $z$  with respect to focus. It is clear that the DH-PSF results in higher and uniform localization precision in all three dimensions than the standard PSF throughout a  $2 \mu\text{m}$  depth of field. However, just near the focal plane, the lateral localization precision of the standard PSF is slightly better than the DH-PSF. This is because the spot size of the standard PSF is smaller than the spot size of the DH-PSF near the focal plane. More importantly, the singularity of the axial localization precision of the standard PSF is not present for the DH-PSF. This singularity is a result of the symmetry of the standard PSF above and below the focal plane and the weak change in the PSF with  $z$  described above.

### 3.2 Comparison between an astigmatic PSF and the DH-PSF for three-dimensional localization

The first method proposed for three-dimensional super-resolution imaging used a cylindrical lens to introduce an astigmatic aberration in the detection path of the microscope.<sup>14, 15</sup> The  $z$  position can then be inferred from the widths of an asymmetric Gaussian fit to the astigmatic PSF. We have performed experiments to compare, based on the number of photons collected, the  $z$  localization precision of both astigmatic imaging and the DH-PSF. In the astigmatic experiment, a 1000 mm focal length cylindrical lens was placed in between the imaging lens and the EMCCD, and the  $4f$  imaging system was removed. The image of 200 nm fluorescent beads emitting at 645 nm was fit to a Gaussian function with independent standard deviations in  $x$  and  $y$  by minimizing the mean-square error between the data and the model function using the MATLAB function, `fminsearch`. The DH-PSF was also fit using `fminsearch`. A calibration curve of the  $x$  standard deviation and the  $y$  standard deviation of the Gaussian fit as a function of  $z$  position was obtained. The ratio of the  $x$  standard deviation to the  $y$  standard deviation was used to obtain a  $z$  position through interpolation from the calibration curve. As can be seen from the data in Figure 9, the astigmatic PSF does not perform as well as the DH-PSF in the  $z$  direction near the focal plane for a given number of detected photons, which in this case is 900-1000 photons per localization. Of course, more sophisticated fitting algorithms could be employed to improve the localization precision,<sup>31</sup> but these would also be expected to improve the precision of the DH-PSF.

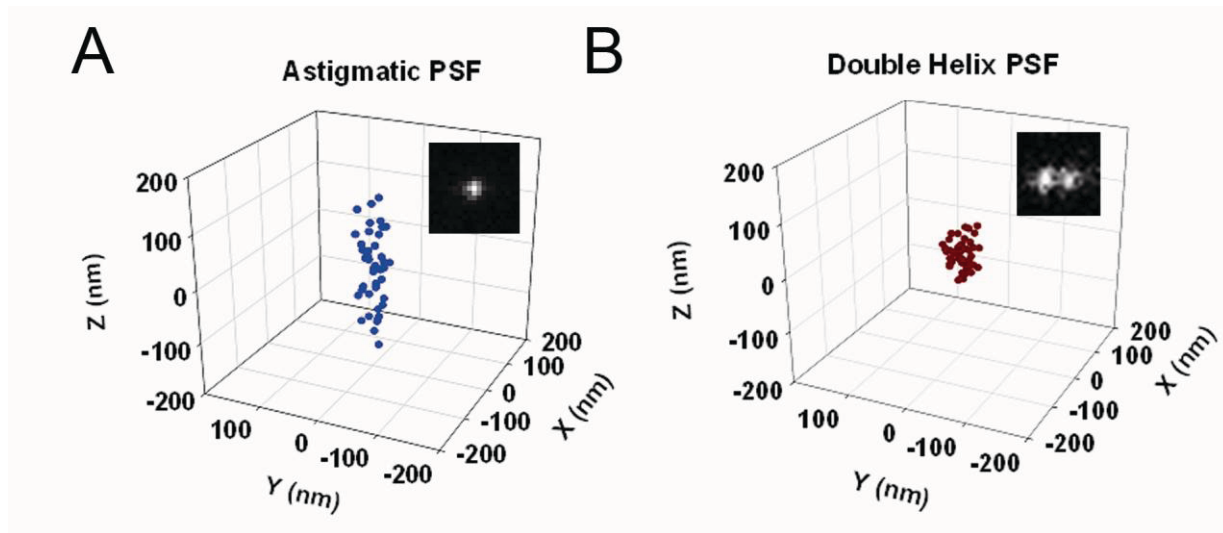


Figure 9. Comparison of localizations made with A) an astigmatic PSF versus B) the DH-PSF for a given number of detected photons. A) The astigmatic PSF was generated with a 1000 mm focal length cylindrical lens. On average, 990 photons were collected per acquisition. The inset shows a typical image from which the position of the bead was obtained. The  $z$  localization precision is 67 nm. B) The DH-PSF has a localization precision of 26 nm in the  $z$  direction for 910 photons detected. This demonstrates that, near the focal plane, the DH-PSF is more useful than the astigmatic PSF for  $z$  localization. For both experiments, a 200 nm fluorescent bead was used as an emitter.

### 3.3 Quantum dot tracking inside living cells

Because of the high localization precision in  $z$  that is affordable with low photon budgets, the DH-PSF is ideally suited to three-dimensional single particle-tracking applications. We have used the DH-PSF to image quantum dots (QTracker 655, Invitrogen) with high spatial and temporal resolution both in 80% glycerol/ $H_2O$  solution and in live COLO205 cells. Figure 10 shows results from the single quantum dot tracking experiments. The stock solution of the quantum dots was diluted to a concentration of 0.1 nM in 80% glycerol/water and sonicated for 1 hour to reduce the number of aggregates. In order to make sure that we are analyzing the tracks from single quantum dots and not aggregates, only traces that showed on/off fluorescence intermittency (blinking) were analyzed. The quantum dots were pumped with an irradiance of  $100 \text{ kW/cm}^2$  with a 561 nm diode laser (Crystalaser, 25 mW). The emission light was filtered by both a dichroic mirror and a long pass filter (Semrock BLP01-561R). The refractive index of the immersion oil on the objective is 1.518, while the refractive index of the glycerol solution is 1.44. We have rescaled the  $z$  values by the factor  $n_{\text{solution}}/n_{\text{oil}}$  to account for this index difference.<sup>35</sup> Figure 10 shows the results of the experiments.

The mean-squared displacement (MSD) of 5 quantum dots was found for short lag times in the 3D Euclidean displacement vector  $\mathbf{r}$ . For a lag time,  $t_{lag}$ , the 3D MSD is defined by (with  $\langle \rangle$  denoting time average)

$$MSD(t_{lag}) = \left\langle \left| \mathbf{r}(t + t_{lag}) - \mathbf{r}(t) \right|^2 \right\rangle. \quad (7)$$

For purely diffusive motion with an uncertainty in the measurement  $\sigma$  at each time point (due mostly to limited photon counts and motion during the acquisition time), the MSD scaling versus  $t_{lag}$  is given by

$$MSD(t_{lag}) = 2nDt_{lag} + \sum_i^n 2\sigma_i^2, \quad (8)$$

where  $D$  is the diffusion coefficient,  $n$  is the number of dimensions, and  $\sigma_i$  is the position uncertainty in each dimension. Figure 10C shows a plot of the MSD in  $\mathbf{r}$  versus lag time averaged over the trajectories of 5 different quantum dots. A fit to the MSD for  $\mathbf{r}$  is also shown in Figure 10C. The diffusion coefficient  $D$  obtained from the slope was found to be  $0.2 \mu\text{m}^2/\text{s}$ . Using the Einstein-Smoluchowski relation for a spherical particle and parameter values for the viscosity of the 80% glycerol solution at 296 K of  $\sim 50$  cP, we obtained a hydrodynamic radius of 21 nm for the individual quantum dots.

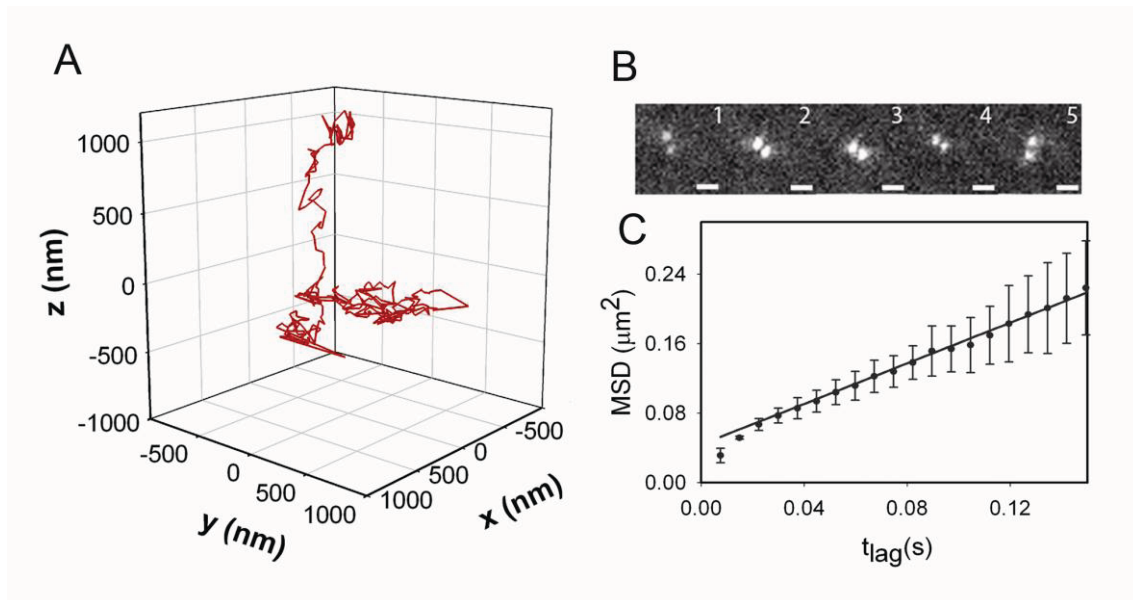


Figure 10. Tracking of a single quantum dot emitter in an 80% glycerol solution. (A) A representative 293-step trajectory taken with 7.5 ms integration time. (B) Images of quantum dots at times of 7.5 ms, 0.56 s, 1.12 s, 1.68 s, and 2.22 s for images 1, 2, 3, 4, and 5, respectively. Scale bar is 1  $\mu\text{m}$ . (C) Plot of the mean-square displacement in  $\mathbf{r}$  for the average of 5 different single quantum dots. A fit to the MSD for displacement  $\mathbf{r}$  gives a diffusion coefficient of  $0.2 \mu\text{m}^2/\text{s}$ .

Imaging in live cells is often complicated by refractive index mismatches and autofluorescent background. Since the ultimate goal of the DH-PSF imaging is three-dimensional imaging of live cells, we decided to test the viability of the method in tracking quantum dots in live cells. We incubated COLO205 cells with 1 nM QTracker (Invitrogen) quantum dots and peptide carrier for 1 hour, followed by three washes with PBS pH 7.4 buffer. The COLO205 cells are approximately 8-10  $\mu\text{m}$  in diameter, which is a thicker sample than any sample previously studied with the DH-PSF. The imaging buffer is pH 7.4 PBS and the quantum dots are being excited with a 561 nm diode laser at an irradiance of  $\sim 10 \text{ kW}/\text{cm}^2$ . In Figure 11A, images at different time points displaying a well-formed DH-PSF are displayed. Figure 11B shows a typical image of what is most likely a vesicle containing several endocytosed quantum dots. The motion of the intracellular structure typically followed a slow, nondiffusive path. Thus, data were taken with time-lapse imaging with 0.1 s exposures every 1 s. On average, 3200 photons were detected per frame with a background noise of 5 photons/pixel/frame most likely resulting from autofluorescent pumping of cellular structures. In Figure 11C, the entire

track, which lasted 98 s, is shown. Symbols representing the acquisitions in Figure 11A are shown on the track in Figure 11C. For this demonstration, we assume that the cell had the same refractive index as water to extract the  $z$  position of the emitter; since no quantification of the track dynamics is performed, this is a reasonable assumption. Based on this experiment, the DH-PSF is a viable method for live cell tracking experiments. Since we are using adaptive optics to form the DH-PSF, it should also be possible in the future to correct for any aberrations, due to index mismatch within the sample, by using the SLM<sup>36</sup> to produce a more perfect DH-PSF.

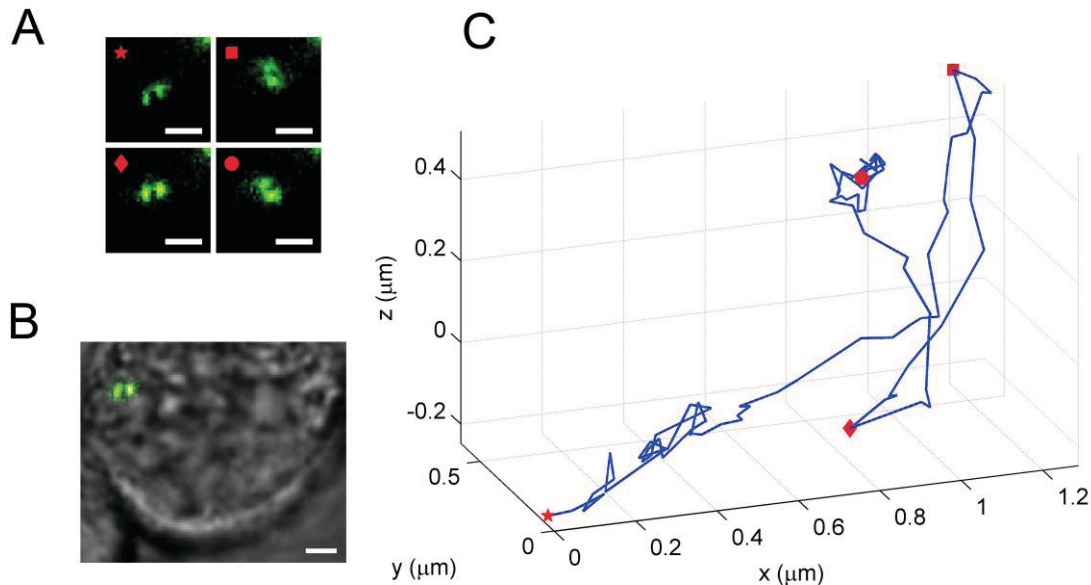


Figure 11. Tracking a quantum dot-labeled structure in a live cell in 3D. (A) Images taken of the structure at different points along the trajectory showing different  $z$  positions. The bright aggregate in the top-right corner should be ignored. (B) Fluorescence image of the emitter overlaid on a white light image of the COLO205 cell (scale bar is 2  $\mu\text{m}$ ). (C) Three-dimensional plot of the labeled structure's trajectory, showing a variety of diffusive and linear transport characteristics. Points on the curve that correspond to the images in (A) are shown by red shapes. An average of 3200 photons/frame with a background noise of 5 photons/pixel/frame was measured for this trajectory.

## 4. CONCLUSION

In conclusion, we have shown in detail why the DH-PSF is far more suitable for three-dimensional superresolution fluorescence imaging than the standard point spread function of a conventional microscope. The DH-PSF contains higher and more uniform Fisher information than the standard PSF over a 2  $\mu\text{m}$  depth of field. In addition, we have shown that the DH-PSF can achieve greater  $z$  localization precision than the astigmatic PSF near the focal plane for a given amount of detected photons. To prove that the DH-PSF is useful for dim emitters in biological environments, we have imaged quantum dots in glycerol solution and in live cells. On the basis of these experiments, we believe that the DH-PSF is a viable candidate for three-dimensional superresolution studies of biological phenomena.

## ACKNOWLEDGEMENTS

We thank R. Piestun and S. R. P. Pavani for providing the DH-PSF phase mask. We are grateful to Julie Biteen, Randall Goldsmith, and Steven Lee for helpful discussions. Hsiao-lu Lee cultured the COLO205 cells used in this work. This work was supported in part by Grant Number R01GM085437 from the National Institute of General Medical Sciences. M.D.L. and M.A.T. acknowledge support from National Science Foundation Graduate Research Fellowships. M.D.L. is

also supported by a 3Com Corporation Stanford Graduate Fellowship, and M.A.T. is also supported by a Bert and DeeDee McMurtry Stanford Graduate Fellowship.

## REFERENCES

- [1] Heimstadt, O. "Das Fluoreszenzmikroskop," *Z. Wiss. Mikrosk.* 28, 330-337 (1911).
- [2] Thompson, R. E., Larson, D. R. and Webb, W. W. "Precise nanometer localization analysis for individual fluorescent probes," *Biophys. J.* 82, 2775-2783 (2002).
- [3] Ober, R. J., Ram, S. and Ward, E. S. "Localization accuracy in single-molecule microscopy," *Biophys. J.* 86, 1185-1200 (2004).
- [4] Bobroff, N. "Position measurement with a resolution and noise-limited instrument," *Rev. Sci. Instrum.* 57, 1152-1157 (1986).
- [5] Yildiz, A., Forkey, J. N., McKinner, S. A., Ha, T., Goldman, Y. E. and Selvin, P. R. "Myosin V walks hand-over-hand: Single fluorophore imaging with 1.5-nm localization," *Science* 300, 2061-2065 (2003).
- [6] Kim, S. Y., Gitai, Z., Kinkhabwala, A., Shapiro, L. and Moerner, W. E. "Single molecules of the bacterial actin MreB undergo directed treadmilling motion in *Caulobacter crescentus*," *Proc. Nat. Acad. Sci. U. S. A.* 103(29), 10929-10934 (2006).
- [7] Biteen, J. S., Thompson, M. A., Tselentis, N. K., Shapiro, L. and Moerner, W. E. "Superresolution Imaging in Live *Caulobacter Crescentus* Cells Using Photoswitchable Enhanced Yellow Fluorescent Protein," *Proc. SPIE* 7185, 71850I (2009).
- [8] van Oijen, A. M., Köhler, J., Schmidt, J., Müller, M. and Brakenhoff, G. J. "3-Dimensional super-resolution by spectrally selective imaging," *Chem. Phys. Lett.* 292, 183-187 (1998).
- [9] Betzig, E., Patterson, G. H., Sougrat, R., Lindwasser, O. W., Olenych, S., Bonifacino, J. S., Davidson, M. W., Lippincott-Schwartz, J. and Hess, H. F. "Imaging intracellular fluorescent proteins at nanometer resolution," *Science* 313(5793), 1642-1645 (2006).
- [10] Hess, S. T., Girirajan, T. P. K. and Mason, M. D. "Ultra-high resolution imaging by fluorescence photoactivation localization microscopy," *Biophys. J.* 91, 4258-4272 (2006).
- [11] Rust, M. J., Bates, M. and Zhuang, X. "Sub-diffraction-limit imaging by stochastic optical reconstruction microscopy (STORM)," *Nat. Methods* 3, 793-795 (2006).
- [12] Greengard, A., Schechner, Y. Y. and Piestun, R. "Depth from Diffracted Rotation," *Opt. Lett.* 31(2), 181-183 (2006).
- [13] Ram, S., Prabhat, P., Chao, J., Ward, E. S. and Ober, R. J. "High accuracy 3D quantum dot tracking with multifocal plane microscopy for the study of fast intracellular dynamics in live cells," *Biophys. J.* 95, 6025-6043 (2008).
- [14] Huang, B., Wang, W., Bates, M. and Zhuang, X. "Three-Dimensional Super-Resolution Imaging by Stochastic Optical Reconstruction Microscopy," *Science* 319, 810-813 (2008).
- [15] Holtzer, L., Meckel, T. and Schmidt, T. "Nanometric three-dimensional tracking of individual quantum dots in cells," *Appl. Phys. Lett.* 90, 053902 (2007).
- [16] Kao, H. P., Verkman, A. S. "Tracking of single fluorescent particles in three dimensions: use of cylindrical optics to encode particle position," *Biophysical Journal* 67, 1291-1300 (1994).
- [17] Ram, S., Chao, J., Prabhat, P., Ward, E. S. and Ober, R. J. "A novel approach to determining the three-dimensional location of microscopic objects with applications to 3D particle tracking," *Proc. SPIE* 6443, 64430D-1-64430D-7 (2007).
- [18] Juette, M. F., Gould, T. J., Lessard, M. D., Mlodzianoski, M. J., Nagpure, B. S., Bennett, B. T., Hess, S. T. and Bewersdorf, J. "Three-dimensional sub-100 nm resolution fluorescence microscopy of thick samples." *Nat. Meth.* 5, 527-529 (2008).
- [19] Sun, Y., McKenna, J. D., Murray, J. M., Ostep, E. M. and Goldman, Y. E. "Parallax: High Accuracy Three-Dimensional Single Molecule Tracking Using Split Images," *Nano Letters* 9(7), 2676-2682 (2009).
- [20] Shtengel, G., Galbraith, J. A., Galbraith, C. G., Lippincott-Schwartz, J., Gillette, J. M., Manley, S., Sougrat, R., Waterman, C. M., Kanchanawong, P., Davidson, M. W., Fetter, R. D. and Hess, H. F. "Interferometric fluorescent

- super-resolution microscopy resolves 3D cellular ultrastructure," *Proceedings of the National Academy of Sciences* 106(9), 3125-3130 (2009).
- [21] v. Middendorff, C., Egner, A., Geisler, C., Hell, S. W. and Schönle, A. "Isotropic 3D Nanoscopy based on single emitter switching," *Opt. Express* 16(25), 20774-20788 (2008).
- [22] Cang, H., Wong, C. M., Xu, C. S., Rizvi, A. H. and Yang, H. "Confocal three dimensional tracking of a single nanoparticle with concurrent spectroscopic readouts," *Appl. Phys. Lett.* 88, 223901 (2006).
- [23] Lessard, G. A., Goodwin, P. M. and Werner, J. H. "Three-dimensional tracking of individual quantum dots," *Appl. Phys. Lett.* 91(22), 224106-3 (2007).
- [24] McHale, K., Berglund, A. J. and Mabuchi, H. "Quantum Dot Photon Statistics Measured by Three-Dimensional Particle Tracking," *Nano Letters* 7(11), 3535-3539 (2007).
- [25] Pavani, S. R. P., Thompson, M. A., Biteen, J. S., Lord, S. J., Liu, N., Twieg, R. J., Piestun, R. and Moerner, W. E. "Three-dimensional, single-molecule fluorescence imaging beyond the diffraction limit by using a double-helix point spread function," *Proc. Nat. Acad. Sci. U. S. A.* 106(9), 2995-2999 (2009).
- [26] Thompson, M. A., Lew, M. D., Badieirostami, M. and Moerner, W. E. "Localizing and Tracking Single Nanoscale Emitters in Three Dimensions with High Spatiotemporal Resolution Using a Double-Helix Point Spread Function," *Nano Lett.* 10(1), 211-218 (2010).
- [27] Pavani, S. R. P., Piestun, R. "High-efficiency rotating point spread functions," *Opt. Express* 16, 3484-3489 (2008).
- [28] Pavani, S. R. P., Piestun, R. "Three dimensional tracking of fluorescent microparticles using a photon-limited double-helix response system," *Opt. Express* 16, 22048-22057 (2008).
- [29] Pavani, S. R. P., Greengard, A. and Piestun, R. "Three-dimensional localization with nanometer accuracy using a detector-limited double-helix point spread function system," *Appl. Phys. Lett.* 95, 021103-1-021103-3 (2009).
- [30] Pavani, S. R. P., DeLuca, J. G. and Piestun, R. "Polarization sensitive, three-dimensional, single-molecule imaging of cells with a double-helix system," *Opt. Express* 17(22), 19644-19655 (2009).
- [31] Mlodzianoski, M. J., Juette, M. F., Beane, G. L. and Bewersdorf, J. "Experimental characterization of 3D localization techniques for particle-tracking and super-resolution microscopy," *Opt. Express* 17(10), 8264-8277 (2009).
- [32] Goodman, J. W. [Introduction to Fourier Optics], Roberts & Company Publishers, Greenwood Village, CO, 491 (2005).
- [33] Cover, T. M., Thomas, J. A. [Elements of Information Theory], John Wiley & Sons, Inc., Hoboken, NJ, 776 (2006).
- [34] Kay, S. M. [Fundamentals of Statistical Signal Processing: Estimation Theory], Prentice-Hall PTR, Englewood Cliffs, NJ, 625 (1993).
- [35] Wiersma, S. H., Torok, P., Visser, T. D. and Varga, P. "Comparison of different theories for focusing through a plane interface," *J. Opt. Soc. Am. A* 14(7), 1482-1490 (1997).
- [36] Kam, Z., Hanser, B., Gustafsson, M. G. L., Agard, D. A. and Sedat, J. W. "Computational adaptive optics for live three-dimensional biological imaging," *Proc. Natl. Acad. Sci. U. S. A.* 98(7), 3790-3795 (2001).